

X-ray polarization in the soft state of Cyg X-1

A. Niedźwiecki¹ ^{*}, M. Szanecki¹ , A. Veledina^{2,3} , A. A. Zdziarski⁴ , A. Chakraborty¹ , J. Poutanen² ,
P. Lubiński⁵ , and A. Salganik² 

¹ University of Lodz, Pomorska 149/153, 90-236 Łódź, Poland

² Department of Physics and Astronomy, FI-20014 University of Turku, Finland

³ Nordita, KTH Royal Institute of Technology and Stockholm University, Hannes Alfvéns väg 12, SE-10691 Stockholm, Sweden

⁴ Nicolaus Copernicus Astronomical Center, Polish Academy of Sciences, Bartycka 18, PL-00-716 Warszawa, Poland

⁵ Institute of Physics, University of Zielona Góra, Szafrana 4a, PL-65-516 Zielona Góra, Poland

March 2026

ABSTRACT

Aims. We aim to identify the physical mechanism responsible for the observed X-ray emission and polarization of Cyg X-1 in the soft state.

Methods. We perform a detailed spectral analysis of X-ray data obtained by NICER, *NuSTAR*, and *INTEGRAL* during observations simultaneous with *IXPE* on 2023 June 20, supplemented at higher energies with archival *CGRO* data. We develop a new model, `retBB`, that describes thermal disk emission and its returning reflection, and apply it together with accurate models of Comptonization and relativistically broadened reflection. Using the resulting spectral solution, we compute the expected polarization signal and compare it with the *IXPE* measurements.

Results. Our spectropolarimetric modeling shows that the observed polarization is produced by Comptonization in a corona undergoing a semi-relativistic outflow with a velocity of $\approx 0.3c$. Our spectral solutions admit either low or high black-hole spin values, depending on the adopted model setup. However, the observed polarization strongly favors a low spin. At high spin, the polarization angle would inevitably rotate significantly across the energy band, which is not consistent with the observations. Apart from this rotation of the polarization angle, general relativistic effects do not play a significant role in producing the observed polarization. In particular, we find that, at most, returning disk radiation contributes only a minor amount.

Key words. accretion, accretion disks – polarization – stars: black holes – stars: individual: Cyg X-1 – X-rays: binaries

1. Introduction

Relativistic effects play a significant role in shaping the polarization of radiation from a thermal, Keplerian accretion disk orbiting a Kerr black hole (Connors et al. 1980; Laor et al. 1990; Schnittman & Krolik 2009; Loktev et al. 2024). An important aspect of these theoretical predictions is the return of disk radiation to the disk surface due to strong gravitational light bending near the black hole. If the disk surface is ionized, reflection of these returning photons produces a distinct spectral component (Cunningham 1976) that is strongly polarized (at the $\sim 10\%$ level) perpendicular to the disk plane (Agol & Krolik 2000), in contrast to the parallel polarization orientation expected for the direct disk emission from an electron scattering dominated atmosphere. The resulting polarization properties depend sensitively on the black hole spin and have therefore been proposed as a means of diagnosing this parameter (e.g., Schnittman & Krolik 2009; Krawczynski 2012). A key limitation of this concept, however, is that the presence of additional spectral components may mask these characteristic signatures, particularly within the 2–8 keV energy range of the *Imaging X-ray Polarimetry Explorer* (*IXPE*; Weisskopf et al. 2022). The polarization of disk radiation is most readily probed in the soft state of black-hole systems, in which the presence of a thermal disk extending close to the black hole is well established (Zdziarski & Gierliński 2004; Done et al. 2007). However, in accordance with the above reser-

vation, the characteristic imprints on the polarization angle (PA) expected from relativistic effects, or from the interplay between oppositely oriented polarization directions of the direct and reflected returning radiation, have not been observed in current measurements of soft-state polarization (e.g., Marra et al. 2024; Ratheesh et al. 2024; Steiner et al. 2024; Svoboda et al. 2024).

In this work, we focus on Cyg X-1, which – with its well-characterized X-ray spectrum (e.g., Gierliński et al. 1999; Zdziarski et al. 2024), precisely measured distance, and a black-hole mass that is relatively well constrained to within a factor of ~ 2 (Miller-Jones et al. 2021; Ramachandran et al. 2025) – is particularly well suited for studies of accretion physics. Steiner et al. (2024) argue that the soft-state polarization of Cyg X-1 is dominated by returning disk and coronal radiation. If correct, this would provide strong support for a rapidly rotating black hole in this system, since the effect is negligible for slowly spinning black holes. However, attributing the observed polarization signal to this mechanism is uncertain, as even for a maximally spinning black hole, the returning radiation is expected to contribute only a small fraction of the high-energy tail observed in this source. We therefore revisit the analysis of the soft-state spectropolarimetric data of Cyg X-1. Using our new model that includes returning radiation, `retBB`, we find that this effect plays only a minor role and instead explore alternative explanations for the observed polarization.

* andrzej.m.niedzwiecki@gmail.com

2. The data

For the spectral analysis, we use the same data as those of epoch 5 of Steiner et al. (2024), which are from the Neutron Star Interior Composition Explorer (NICER), the *Nuclear Spectroscopic Telescope Array* (*NuSTAR*), and the Imager on Board the INTEGRAL Satellite (IBIS), obtained on 2023 June 20 simultaneously with one of the *IXPE* observations. The IBIS consists of two detectors, ISGRI and PICSiT; here, we use the data from ISGRI. The NICER data are affected by stray sunlight,¹ however, the related problems seem to occur mainly above 6 keV. The data below 6 keV are consistent with the simultaneously acquired *NuSTAR* data and with an earlier NICER observation of Cyg X-1 in the soft state.² Therefore, we restrict the NICER data to the 1–6 keV energy range.

In addition, we use data from the Oriented Scintillation Spectrometer Experiment (OSSE) on board the *Compton Gamma Ray Observatory* (*CGRO*). OSSE observed Cyg X-1 in the soft state twice, in 1994 (Phlips et al. 1996) and 1996 (Gierliński et al. 1999; McConnell et al. 2002). These data extend, with relatively high statistics, beyond the range available to the ISGRI, up to ≈ 600 keV, and the OSSE detector is very well calibrated. We have compared the spectral slopes of the two data sets with those of the ISGRI and found that the 1994 data are very similar (except for normalization), and thus we use them here.

The *IXPE*, NICER, *NuSTAR*, IBIS, and OSSE data used for the spectral analysis are in the 2–8, 1–6, 3–78, 32–220 and 50–600 keV ranges, respectively. During the standard NICER data reduction, the script `nicer13-spect` added a 1.5% systematic error to each channel in the 0.34–9.0 keV range and a 2.5% systematic error beyond that. We have not added any systematic errors to the *NuSTAR* data. The NICER and *NuSTAR* spectral data have been optimally binned (Kaastra & Bleeker 2016) with the additional requirement of at least 20 counts per bin. We have added a 2% systematic error to the IBIS data.

We fit the spectra using `xSPEC` (Arnaud 1996), and report uncertainties at 90% confidence. Differences between the calibrations of different detectors are taken into account by multiplying the model spectra by $KE^{-\Delta\Gamma}$ (using `plabs` in `xSPEC`). We assume $K = 1$ and $\Delta\Gamma = 0$ for the *NuSTAR* FPMA detector, as well as $\Delta\Gamma = 0$ for ISGRI and OSSE (necessary due to the relatively large statistical uncertainties). We set the photon energy grid (as necessary for convolution models) by the `xSPEC` command `energies 0.01 1000 1000 log`. The polarization predicted by our models is compared with the averaged *IXPE* data from seven soft-state observations of Cyg X-1 in 2023 and 2024 reported in Kravtsov et al. (2025).

3. The model

We build the spectral model closely following the treatment of Zdziarski et al. (2024). We adopt the values of the distance to the source $D = 2.22$ kpc and the mass of the BH of $M_{\text{BH}} = 21.2M_{\odot}$ as determined by Miller-Jones et al. (2021); however, considering recent investigation of Ramachandran et al. (2025), who estimated a lower mass range of $M \approx (12.7\text{--}17.8)M_{\odot}$, we also examine how the results depend on the assumed M_{BH} . For the Galactic

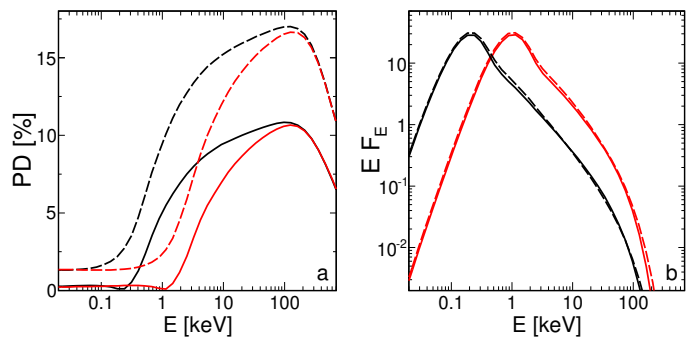


Fig. 1. Spectropolarimetric properties of radiation Comptonized in a slab geometry representing the disk-corona system. (a) Energy dependence of the PD as observed at inclination $i = 35^\circ$ for the outflow velocities $v = 0$ (solid) and $v = 0.3c$ (dashed) and two values of the blackbody temperature of seed photons, $kT_{\text{seed}} = 0.05$ keV (black) and 0.25 keV (red), corresponding to the color temperatures in our fitted disk model at $\approx 100R_g$ and $\approx 10R_g$, respectively. In all cases, the Comptonization parameters are $kT_e = 25$ keV and $\tau = 0.75$, corresponding to the corona parameters found in Sect. 4. (b) The corresponding energy spectra.

absorption, we use `tbabs`, which assumes the abundances from Wilms et al. (2000).

We have developed a new model, `retBB`, for the direct and returning emission from a thermal disk, and we describe and compare it with similar models in Appendix A. We consider disk emission from the innermost stable circular orbit (ISCO) out to 10^3R_g , where $R_g = GM_{\text{BH}}/c^2$. For the Page & Thorne (1974) temperature profile and neglecting the returning radiation, `retBB` is fully consistent with the `kerrbb` model (Li et al. 2005). The models differ in how they treat returning photons, which in `kerrbb` are assumed to be completely absorbed and thereby increase the local temperature of the disk, whereas `retBB` accounts for their reflection. The reflection of blackbody photons is computed using the `xillverNS` tables developed for that case by García et al. (2022). To enable comparison with other models, `retBB` also allows for a fully elastic reflection. This is computed using the formalism of Chandrasekhar (1960). In the `xSPEC` implementation of either version of the model, we only consider the first-order returning photons. The contribution from higher orders is small (see Appendix A for details), and including it would make the model very slow. Moreover, there are no publicly available opacity tables suitable for higher reflection orders. `retBB` is parametrized by the black hole mass M_{BH} and spin a , accretion rate \dot{M} , inclination angle i , and the spectral hardening factor, $f_{\text{col}} = T_{\text{col}}/T_{\text{eff}}$, where T_{col} is the local color temperature and $T_{\text{eff}} = (\mathcal{F}/\sigma_{\text{SB}})^{1/4}$ is the effective temperature, where \mathcal{F} is the local radiation flux and σ_{SB} is the Stefan-Boltzmann constant. For the `xillverNS` reflection, the disk surface is characterized by the ionization parameter, ξ , iron abundance, Z_{Fe} , and density, n . The last parameter is allowed to vary in the range $10^{16}\text{--}10^{18}\text{ cm}^{-3}$. Although `xillverNS` covers a broader range of densities, we have verified that for $n < 10^{16}\text{ cm}^{-3}$ and $n > 10^{18}\text{ cm}^{-3}$ the model fails to conserve energy (in the sense that the angle-averaged reflected energy exceeds the incident energy).

Following Zdziarski et al. (2024), we consider possible dissipation in surface layers of the disk. We model this by fully covering the disk by a warm scattering corona with $kT_e \sim 1$ keV and $\tau \gg 1$. To do so, we use the `thcomp` code (Zdziarski et al. 2020) with free kT_e and τ .

Cyg X-1 in the soft state shows relatively strong high-energy tails (e.g., Gierliński et al. 1999; McConnell et al. 2002). They

¹ <https://heasarc.gsfc.nasa.gov/docs/nicer/>

² We applied the model developed here to the simultaneous NICER/*NuSTAR* observations of Cyg X-1 obtained in 2019 and recovered the same accretion disk parameters as in the present analysis, with a similar pattern of residuals to those shown in Fig. 3 for the current NICER data.

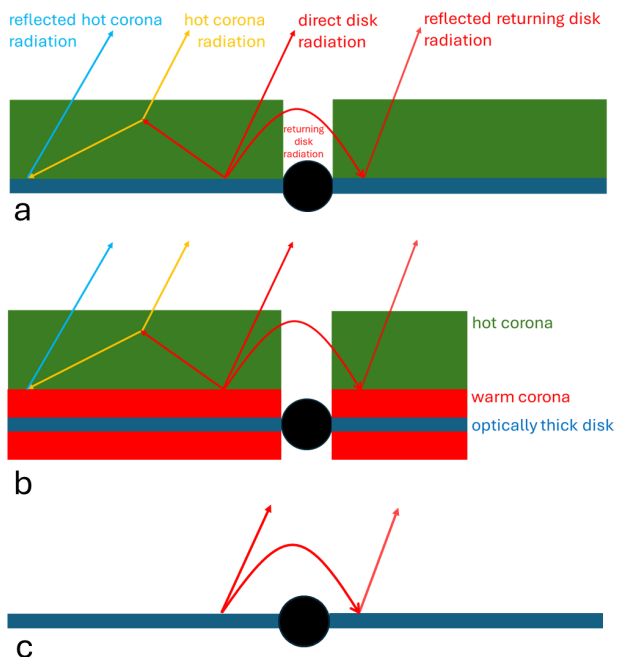


Fig. 2. Geometries considered in this work and the main spectral components produced close to the black hole. (a) Geometry considered in models 1 and 2. (b) Geometry with an additional warm corona considered in model 3. (c) ‘No-corona’ geometry considered in model 4.

are most likely produced by Comptonization by electrons in a hot corona above the disk. We assume the seed photons are from the disk emission. We use a convolution Comptonization code allowing for the electron distribution to be hybrid, i.e., Maxwellian with a high-energy tail, `comppsc`,³ which is a convolution version of the `compps` iterative-scattering code (Poutanen & Svensson 1996). The present model approximates the high-energy tail as a power law in the electron momentum, parametrized by its index, p , and the minimum and maximum Lorentz factors, γ_{\min} and γ_{\max} , respectively. The Maxwellian and the power law intersect at γ_{\min} . The other parameters are kT_e and τ . We assume a slab geometry, and we describe the covering fraction of the disk surface by the corona by f_{sc} .

To compute the reflected/reprocessed spectrum, we use the convolution model, `xilconv`, developed by C. Done following the methodology of Kolehmainen et al. (2011). It is based on the `xillver` opacity tables of García et al. (2013) and the Greens functions of Magdziarz & Zdziarski (1995). The ξ and Z_{Fe} parameters of `xilconv` and `relconv` are linked in our models. However, `xilconv` allows the ionization parameter to vary in the range $0 \leq \log_{10} \xi_{\text{xil}} \leq 4.7$, whereas in `xillverNS` $0 \leq \log_{10} \xi_{\text{ret}} \leq 4$; therefore, we use $\log_{10} \xi_{\text{ret}} = \min(4, \log_{10} \xi_{\text{xil}})$. We also note that `xilconv` assumes $n = 10^{15} \text{ cm}^{-3}$, which is beyond the range of densities permitted in `relconv`. The reflection features are relativistically broadened, which we treat by using the convolution model `relconv` (Dauser et al. 2010). That model assumes a power-law radial distribution of the irradiation, $\propto R^{-\beta}$, and we allow for β to be a free parameter. The reflection features are relativistically broadened, which we treat using the convolution model `relconv` (Dauser et al. 2010). This model assumes a power-law radial distribution of the disk irradiation, $\propto R^{-\beta}$, and we allow β to be a free parameter. Although the coronal emission approximately follows the radial dependence

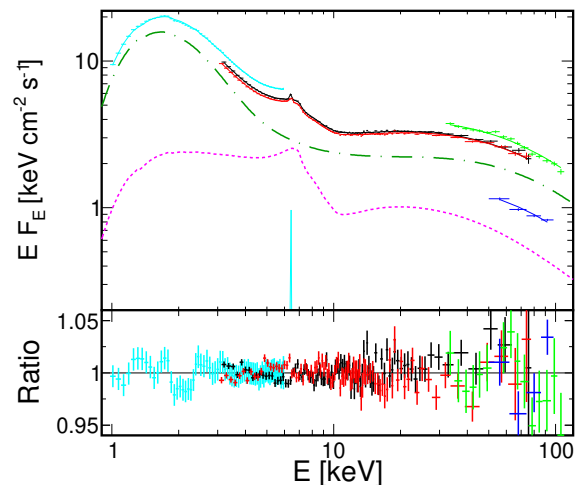


Fig. 3. Spectral energy distribution of Cyg X-1. Top: the NICER (cyan), *NuSTAR* (black and red), *INTEGRAL* (green) and *CGRO* (blue) unfolded spectra for model 2. The dot-dashed (green), dotted (magenta), and solid (cyan) curves show the absorbed Comptonized component (including unscattered seed photons from the thermal disk), coronal reflection from accretion disk, and static reflection, respectively; see Table 1 for the definition of spectral components. The spectral components are normalized to NICER. Bottom: the data-to-model ratios.

of the disk through the seed-photon input, the resulting reflection can deviate from this dependence because of corona-to-disk transfer effects. These may include relativistic energy shifts and light bending, in particular the return of coronal radiation initially emitted away from the disk. Such effects are not explicitly modeled here and are therefore effectively absorbed into the fitted value of β . The other `relconv` parameters, a and i , are linked to `relBB`. We assume the inner radius of the reflection emission to be at the ISCO. We take into account the scattering of the reflected photons in the hot corona. Normalization of the reflected relative to the incident spectrum is given by the scaling parameter, \mathcal{R} , which for `xilconv` is defined in the same way as in `ireflect`.

Cyg X-1 also exhibits a weak, narrow Fe $K\alpha$ line, with an equivalent width of ≈ 10 eV, which may be produced by reflection from the surface of the donor (Walton et al. 2016). We describe it by setting $\xi_{\text{xil}} = 1$ in `xilconv`, and we refer to this component as the static reflection.

We characterize polarization by the polarization degree and angle, $\text{PD} = (q^2 + u^2)^{1/2}$ and $\text{PA} = 0.5 \text{atan2}(u/q)$, where $q = Q/I$ and $u = U/I$ are the normalized Stokes parameters (Chandrasekhar 1960). We adopt the IAU definition, with PA measured counterclockwise in the image plane from the projection of the black-hole spin axis. In this convention, polarization parallel to the disk plane corresponds to $\text{PA} = \pm 90^\circ$. Furthermore, we use a clockwise sense of disk rotation for comparison with Cyg X-1, consistent with the system clockwise orbital motion (Miller-Jones et al. 2021), whereas most theoretical studies adopt a counterclockwise disk rotation with respect to the observer. However, following the standard practice in X-ray studies of Cyg X-1, we give inclination angles $i < 90^\circ$. In the standard binary-system convention, in which clockwise orbits have inclinations $> 90^\circ$, this corresponds to an orbital inclination of $180^\circ - i$.

We assume that the polarization of the direct disk emission is described by the results of a plane-parallel, electron-scattering dominated atmosphere (Chandrasekhar 1960; Sobolev

³ https://github.com/mitsza/comppsc_conv

Table 1. The model definitions and the fitted parameter values.

Models 1,2,5: <code>plabs.tbabs.(relconv.comppsc.xilconv.comppsc.retBB+comppsc.retBB + xilconv.comppsc.retBB)</code>						
Model 3: <code>plabs.tbabs.(relconv.comppsc.xilconv.comppsc.thcomp.retBB</code>						
<code>+comppsc.thcomp.retBB + xilconv.comppsc.thcomp.retBB)</code>						
Model 4: <code>plabs.tbabs.(retBB + xilconv.retBB)</code>						
		model 1	model 2	model 3	model 4	model 5
<code>tbabs</code>	N_{H} [10^{21} cm^{-2}]	$7.6^{+0.1}_{-0.1}$	$7.6^{+0.1}_{-0.1}$	$8.5^{+0.1}_{-0.1}$	$6.4^{+0.2}_{-0.2}$	$7.0^{+0.1}_{-0.1}$
<code>disk</code>	\dot{M} [10^{18} g s^{-1}]	$0.20^{+0.01}_{-0.01}$	$0.20^{+0.03}_{-0.01}$	$0.49^{+0.04}_{-0.05}$	$0.24^{+0.03}_{-0.04}$	$0.21^{+0.01}_{-0.01}$
	a	$0.99^{+0.01}_{-0.03}$	$0.99^{+0.01}_{-0.01}$	$0^{+0.2}_{-0}$	$0.998^{+0}_{-0.001}$	$0.98^{+0.01}_{-0.03}$
	i [deg]	35^{+1}_{-1}	35^{+1}_{-1}	35^{+1}_{-1}	35^{+3}_{-5}	31^{+3}_{-2}
	f_{col}	$1.5^{+0.1}_{-0.1}$	$1.5^{+0.1}_{-0.1}$	$1.5^{+0.1}_{-0.3}$	$1.7^{+0.1}_{-0.1}$	$1.7^{+0.2}_{-0.1}$
	Z_{Fe}	–	$5.7^{+0.3}_{-0.6}$	$6.0^{+0.3}_{-0.7}$	10^{+0}_{-2}	$2.8^{+0.4}_{-0.4}$
	$\log_{10} \xi$	–	$4.0^{+0}_{-0.1}$	$4.0^{+0}_{-0.1}$	4^{+0}_{-1}	4^{+0}_{-0}
	$\log_{10} n$	–	18^{+0}_{-2}	18^{+0}_{-2}	18^{+0}_{-1}	16^{+2}_{-0}
	<code>hot corona</code>	kT_e [keV]	25^{+4}_{-2}	25^{+2}_{-1}	24^{+2}_{-1}	–
τ		$0.77^{+0.05}_{-0.05}$	$0.77^{+0.05}_{-0.05}$	$0.75^{+0.11}_{-0.05}$	–	$2.8^{+0.1}_{-0.3}$
p		$1.0^{+0.5}_{-0}$	$1.0^{+0.1}_{-0}$	$1.1^{+0.2}_{-0.1}$	–	$1.0^{+0.5}_{-0}$
γ_{min}		$1.4^{+0.1}_{-0.1}$	$1.4^{+0.1}_{-0.1}$	$1.5^{+0.2}_{-0.1}$	–	$1.2^{+0.2}_{-0.1}$
γ_{max}		$5.1^{+0.2}_{-0.1}$	$5.1^{+0.1}_{-0.1}$	$5.5^{+0.1}_{-0.1}$	–	17^{+1}_{-1}
f_{sc}		$0.43^{+0.04}_{-0.04}$	$0.43^{+0.03}_{-0.05}$	$0.41^{+0.03}_{-0.05}$	–	$0.013^{+0.003}_{-0.004}$
<code>warm corona</code>		τ	–	–	23^{+4}_{-3}	–
	kT_e [keV]	–	–	$0.49^{+0.01}_{-0.02}$	–	–
<code>relat. refl.</code>	\mathcal{R}	$0.34^{+0.03}_{-0.02}$	$0.34^{+0.04}_{-0.02}$	$0.31^{+0.02}_{-0.02}$	–	$7.0^{+0.5}_{-0}$
	a	$0.99^{+0.01}_{-0.03}$ (l)	$0.99^{+0.01}_{-0.01}$ (l)	$0^{+0.2}_{-0}$ (l)	–	$0.98^{+0.01}_{-0.03}$ (l)
	i [deg]	35^{+1}_{-1} (l)	35^{+1}_{-1} (l)	35^{+1}_{-1} (l)	–	31^{+3}_{-2} (l)
	β	$2.8^{+0.1}_{-0.1}$	$2.8^{+0.1}_{-0.1}$	$4.0^{+0.2}_{-0.3}$	–	$2.0^{+0.1}_{-0.2}$
	Z_{Fe}	$5.7^{+0.3}_{-0.7}$	$5.7^{+0.3}_{-0.6}$ (l)	$6.0^{+0.3}_{-0.7}$ (l)	–	$2.8^{+0.4}_{-0.4}$ (l)
	$\log_{10} \xi$	$4.0^{+0.1}_{-0.2}$	$4.0^{+0.1}_{-0.1}$ (l)	$4.1^{+0.1}_{-0.2}$ (l)	–	$4.37^{+0.02}_{-0.02}$ (l)
	<code>static refl.</code>	\mathcal{R}	$0.05^{+0.01}_{-0.01}$	$0.05^{+0.01}_{-0.01}$	$0.04^{+0.01}_{-0.01}$	< 1
χ^2_{ν}		665/637	660/636	654/634	536902/170	761/636

Notes. `retBB` uses elastic reflection in model 1 and `xilverNS` in models 2–5. Models 1, 2, 3 and 5 are fitted to the NICER, *NuSTAR*, ISGRI, and OSSE data. Model 4 is fitted to NICER and *NuSTAR* only. For models 1–3 and 5, the first term in parentheses represents the relativistic reflection (dotted magenta curves in Figs. 3, 4, and 5), the second term is the sum of hot-corona Comptonization and unscattered thermal disk emission (including reflected returning radiation), and the third term corresponds to static reflection. In all models $M_{\text{BH}} = 21.2M_{\odot}$ and $D = 2.22 \text{ kpc}$. (l) denotes a linked parameter; the ξ parameters given in the ‘disk’ and ‘relativistic reflection’ sections differ due to limitations of `xilverNS`, see text. In model 5 we use constrain $\mathcal{R} \geq 7$.

1963). The same assumption is adopted for the model including a warm corona, in which the direct component is computed as `thcomp-retBB`. The polarization of the reflected components is calculated using the formalism of Chandrasekhar (1960) for reflection from an electron-scattering dominated slab. For the reflection of the hot-corona radiation, modeled as `xilconv-comppsc`, we assume locally isotropic irradiation of the disk surface, whereas for the returning-radiation component in `retBB` we account for the full angular dependence of the incident flux.

The polarization of the hot-corona emission is computed using a newly developed version of `compps` (Poutanen & Svensson

1996; Poutanen et al. 2023), which treats the polarization of Comptonized radiation produced in a slab geometry irradiated from below. The version of the model employed here allows only for a thermal electron distribution; consequently, polarization arising from the non-thermal component of the fitted hybrid electron distribution is neglected. In calculating the polarization of this component, we assume that the corona corotates with the disk and that the radius-dependent seed-photon input is described by a blackbody spectrum with the disk’s local color temperature. We also take into account motion in the corona away from the disk, which was previously found to be required to reproduce the observed hard-state polarization (Poutanen et al.

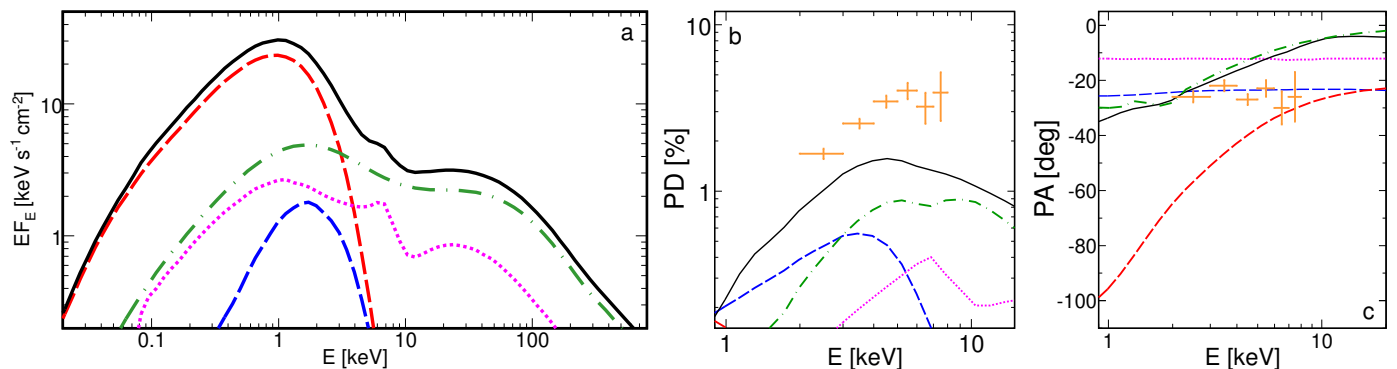


Fig. 4. Unabsorbed spectral components and polarization properties of model 2 involving a rapidly rotating black hole. Polarization is calculated neglecting an outflow (i.e., $v = 0$). The orange points in panels (b) and (c) show the average PD and PA measured by *IXPE* in the soft state of Cyg X-1 (Kravtsov et al. 2025). (a) The total spectrum (solid black curve) and individual spectral components of model 2; the direct thermal disk emission, reflected returning radiation, hybrid Comptonized emission, and its reflection are shown by dashed red, dashed blue, dot-dashed green, and dotted magenta curves, respectively. (b) The polarization degree. The solid black curve shows the net PD resulting from the combined polarization signals of all components, while the colored curves show the contributions of the polarized part of each component to the total flux. (c) The polarization angle, measured counterclockwise from celestial North. For the PA calculation, we assume that the disk rotates clockwise and that the disk axis is aligned with the radio jet, adopting a position angle of $-23^\circ.5$. The line styles and colors in panels (b) and (c) correspond to those used in panel (a).

2023), and also appears necessary to account for the observed soft-state polarization within our best-fitting spectral model. The outflow velocity measured in the corona frame is denoted by v . Figure 1 illustrates the dependence of the PD on the seed-photon temperature and the outflow velocity. For $v = 0$, first-order scattering produces radiation weakly polarized parallel to the slab, while higher-order scatterings yield perpendicular polarization with PD increasing with energy. For $v = 0.3c$, the radiation is polarized perpendicular to the slab at all energies and the PD is higher than in the static case. A detailed discussion of the underlying physical mechanisms can be found in Poutanen et al. (2023). In our modeling, the spectral solution is obtained assuming a static corona, and the outflow is included only in the polarization calculations. This is justified for the semi-relativistic velocity considered here, as illustrated in Fig. 1. While $v = 0.3c$ significantly increases the PD, the corresponding change in the total radiation spectrum is negligible.

The procedures described above yield the local polarization of the reflected, Comptonized, and direct disk radiation. The transfer functions defined in Appendix A are then applied to compute the polarized fluxes of those components received by a distant observer.

4. Results

4.1. Spectral decomposition

We first attempted to fit the entire energy range of 1–600 keV, but we were unable to fit the range above about 100 keV, where our models overestimated the data. A likely reason for that is that the nonthermal part of the electron distribution is assumed to be a power law with a sharp cutoff, while an exponential type of cutoff is more likely. We have thus opted for fitting the energy range of 1–100 keV only. We have considered models without and with a warm corona, see Fig. 2. The model definitions and fitted parameters are given in Table 1. Figure 3 shows the spectrum and residuals for model 2; for models 1 and 3, these are very similar. Figures 4a and 5a show unabsorbed spectral components of models 2 and 3, respectively.

For the case without a warm corona, we obtained a good fit for $a \approx 0.99$. This high spin implies a relatively strong re-

turning component, accounting for $\sim 5\%$ of the total flux at ~ 2 keV, where its contribution is greatest (see Fig. 4). For the warm-corona case, we also obtained a good fit, but the fitted spin parameter is $a \approx 0$. Consequently, in this case (model 3), the returning component is very weak, contributing less than 1% to the total flux in the whole energy range.

Motivated by the results of Ramachandran et al. (2025), we investigated how our results depend on adopting a lower black-hole mass. For $M_{\text{BH}} = 17M_{\odot}$, we find that the change can be compensated by a reduction of the hardening factor to $f_{\text{col}} \approx 1.3$, yielding a spectral fit of the same quality to that reported in Table 1, and with only insignificant changes in the remaining parameters. Interestingly, the inclination of $i \approx 35^\circ$ fitted in all models is consistent with the binary inclination assessed by Ramachandran et al. (2025). Adopting $i = 27^\circ.5$ in model 3, as estimated by Miller-Jones et al. (2021) for the orbital inclination, yields $\Delta\chi^2 = 17$ relative to our best solution with $i = 35^\circ$.

Steiner et al. (2024) inferred a crucial role for returning disk radiation under the assumption that the disk is perfectly reflecting. This raises the question of whether their conclusions depend on the unity-albedo assumption. We address this issue by comparing the model in which the returning component is computed assuming a unity albedo (as in Steiner et al. 2024, model 1) with the model employing the *xillverNS* tables (model 2). Both model variants provide an equally good description of the data, without requiring changes in the parameters of the other spectral components. This insensitivity is partly due to the high ionization state of the disk surface (required to reproduce the coronal reflection), but primarily to the very weak contribution of the returning component, which is negligible in particular around the Fe $K\alpha$ line.

4.2. Polarization constraints

Based on the spectral descriptions obtained above, we now compute the corresponding polarization signals, initially neglecting any outflow in the corona. As shown in Fig. 4b, the polarization in model 2 is dominated by the Comptonized component; however, the observed PD is underpredicted by a factor of ~ 2 . The reflected returning component contributes $\lesssim 25\%$ to the observed PD around 3 keV, with its contribution rapidly decreasing

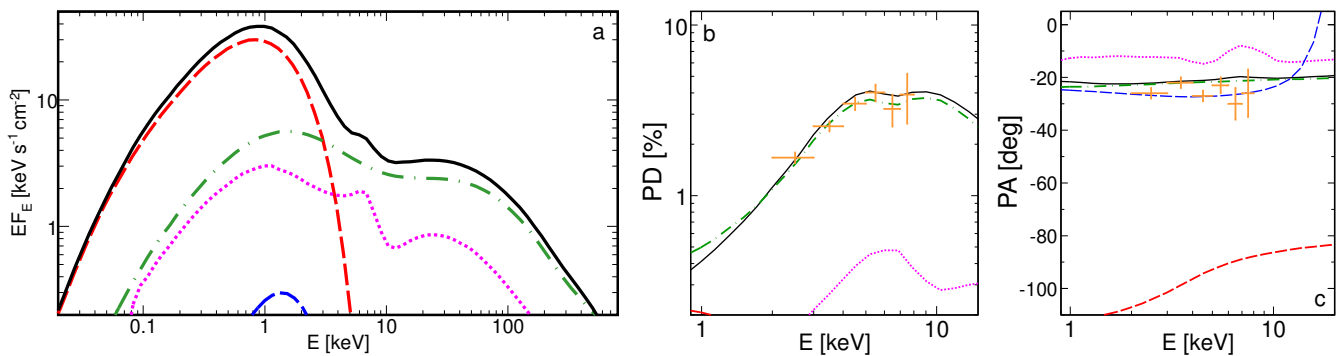


Fig. 5. Same as Fig. 4 but for model 3 with $a = 0$ and including an outflow with $v = 0.3c$. The red dashed curves are for the thermal disk spectrum modified by warm-corona Comptonization.

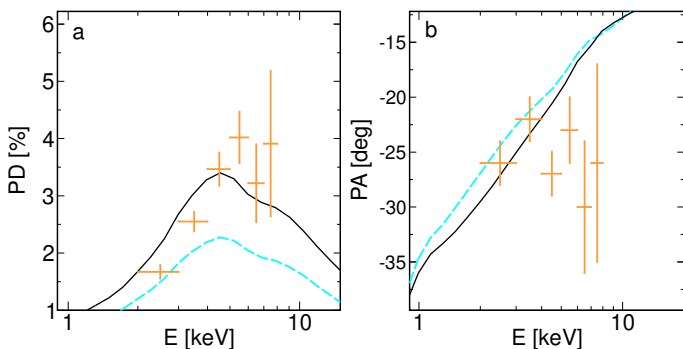


Fig. 6. Polarization degree (a) and angle (b) of model 2 including an outflow with $v = 0.3c$, for $i = 35^\circ$ (the fitted value in this model; dashed cyan curves) and $i = 39^\circ$ (better matching the observed PD; solid black curves).

at higher energies. This weak contribution is readily understood given the small fraction of the total flux provided by this component ($< 5\%$).

The coronal radiation undergoes a significant, energy-dependent rotation of the PA due to special- and general-relativistic effects, which is reflected in the energy dependence of the net PA predicted in this model (see Fig. 4c). For large values of a , the coronal emission contains a strong contribution from small radii ($\lesssim 5R_g$), where these PA rotation effects are most pronounced. The polarized component of the Comptonized emission depends on radius through the radial dependence of the seed-photon temperature (see Fig. 1), and the largest PA rotations are observed at the highest energies (dominated by these small radii). In particular, at the inner edge of the disk, the color temperature reaches $kT_{\text{col}} \simeq 0.6$ keV, so that first-order scattering dominates up to the *IXPE* energy range, and the polarized spectrum rises steeply in this band as the emission transitions to domination by higher-order scatterings.

The effects observed in the PA of the remaining spectral components are comparatively minor, owing to their low contribution to the net polarization. Nevertheless, we discuss them here for completeness. The returning component is produced primarily by reflection of photons emitted near the inner edge of the disk ($\sim 1.5R_g$) and subsequently returning to the disk over a wide range of radii, with the emission/return redshift increasing with the radius at which the photons return. The returning radiation observed below 10 keV is dominated by reflection from radii $\gtrsim 5R_g$, where the relativistic PA rotation is weak and, consequently, the observed polarization of this component is perpendicular to the disk plane. In addition, the associated grazing

irradiation of the disk surface at these radii leads to reflection toward low-inclination observers at scattering angles $\sim \pi/2$ which results in a relatively strong intrinsic polarization of this component, at the level of $\sim 10\%$. On the other hand, our description of the coronal reflection is phenomenological and involves assumptions that tend to reduce the PD. First, we assume locally isotropic irradiation of the disk surface, which produces a less polarized reflected signal for low-inclination observers than grazing illumination. Second, we assume that the rest-frame reflection spectrum is the same at all radii, which leads to partial depolarization through the mixing of radiation whose PAs undergo different relativistic rotations (for the returning radiation, such a depolarizing mixing does not occur because the rest-frame reflection depends on the radius through redshift). Also, mixing of polarization signals with identical rest-frame spectra but differently rotated PA leads to the net rotation by $\simeq -5^\circ$, which is approximately the same at all energies (for the fitted $\beta \simeq 2.8$).

Figure 6 shows the polarization properties of model 2 including an outflow with $v = 0.3c$, and illustrates the dependence on inclination, to which the observed PD is highly sensitive. We see that the predicted PA still exhibits a strong energy-dependent rotation, making it inconsistent with the observed PA. Such behavior is in fact expected for any high-spin model in which the emission follows the radial dissipation profile of a Novikov & Thorne (1973) disk, that is, includes a strong contribution from the innermost few gravitational radii. The mixing of contributions with differently rotated PAs also reduces the net polarization, and for the fitted inclination of $i = 35^\circ$ the observed PD is still under-predicted. The PD can be matched more closely by adopting a larger inclination, $i = 39^\circ$; fixing the inclination in model 2 at this value worsens the fit, yielding $\Delta\chi^2 = 9$.

Figure 5 shows the spectral components and polarization for model 3, which includes a warm corona and a black hole with $a \simeq 0$. However, the polarization calculations implemented in `comps` allow only Planckian seed photons, whereas in model 3 the seed photons follow the spectrum of optically thick Comptonization. We therefore approximate the actual `thcomp-retBB` input with a `retBB` spectrum using a color-correction factor $f_{\text{col}} = 2.8$, chosen to reproduce a similar spectral shape. Consequently, the polarization predictions in this case should be regarded as approximate. Apart from the negligible contribution of returning radiation, the relative roles of the individual components are very similar to those in model 2. As in that model, the observed polarization is dominated by Comptonization in the hot corona and, for $v = 0$ (and $i = 35^\circ$), the predicted polarization is weaker than the *IXPE* measurement. However, the coronal emission is now dominated by radii $\gtrsim 10R_g$, where relativistic effects

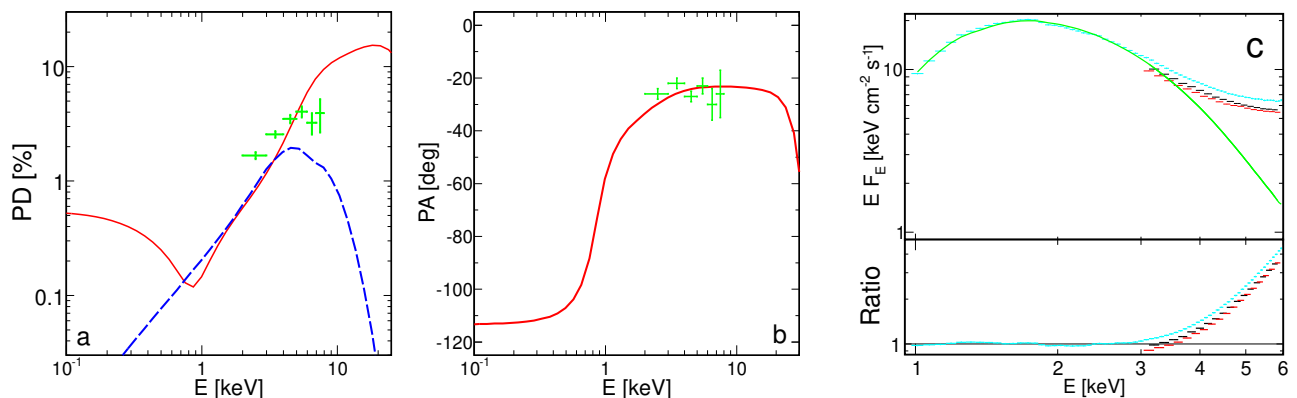


Fig. 7. Comparison of model 4 with the spectropolarimetric data on Cyg X-1. Panels (a) and (b) compare the polarization properties of model 4 (red solid curves), following the assumptions of the ‘no-corona’ model in Steiner et al. (2024) (i.e., including only the thermal disk), with the soft-state *IXPE* data on Cyg X-1. Panel (c) shows an attempt to fit this model to the NICER and *NuSTAR* spectral data, with the observed data shown in cyan, red, and black as in Fig. 3 and the best-fitted model spectrum by the green line in the top, and the data-to-model ratio shown in the bottom. The blue dashed curve in panel (a) shows the contribution to PD of the returning disk component for parameters used in Steiner et al. (2024), see Sect. 4.3.

are weak and the polarization remains approximately perpendicular to the disk plane. Models including a low-spin black hole therefore generally reproduce the observed PA. The weak rotation of PA also implies only weak depolarization due to the mixing of contributions with different PAs. Figure 5 shows predictions for a model with $v = 0.3c$, which in this case reproduces both the observed PD and PA for $i = 35^\circ$. In Fig. 5 we assumed $a = 0$. However, for low values of a the dependence on the exact spin value is weak, and adopting $a = 0.2$ (within the uncertainty range of model 3) yields polarization properties very similar to those obtained for $a = 0$.

Interestingly, the observed PD shows a hint of a decline in the 6–7 keV energy bin, which may be associated with the contribution of Fe $K\alpha$ photons at these energies. The model predicts a similar decline in PD, although its magnitude is underestimated because our treatment assumes that the entire reflected spectrum is polarized perpendicular to the disk, whereas the Fe $K\alpha$ line should instead be polarized parallel to the disk due to scattering of a fraction of fluorescent photons. This effect cannot be consistently captured within reflection models based on the *xillver* tables.

4.3. ‘No-corona’ and reflection-dominated models

The importance of returning radiation in producing the net soft-state polarization of Cyg X-1 was previously supported by considering a model without a Comptonizing corona (Steiner et al. 2024). To address this scenario, we consider model 4, constructed under the same assumptions (see Fig. 2c and the definition in Table 1). Such a configuration does indeed produce a polarization signal consistent with the *IXPE* measurements (the underlying properties of the returning radiation, leading to its high polarization and negligible PA rotation at *IXPE* energies, are discussed above; see also Appendix A), as shown in Fig. 7. However, removing the hot corona, which primarily increases the PD by reducing the total flux, also prevents the model from reproducing the observed high-energy emission. An attempt to fit this configuration to the NICER and *NuSTAR* data is summarized in Table 1, and the severe underprediction of the flux above 3 keV is illustrated in Fig. 7c.

The model that was earlier used to reproduce both the spectrum and polarization (albeit not constrained by a fit to the ob-

served energy spectrum), included a Comptonized emission and its reflection, the latter strongly exceeding the incident emission, by a factor of ≈ 7 (figure 4 in Steiner et al. 2024). A key assumption was that the disk behaved as a perfect reflector. To assess whether such a reflection-dominated scenario is compatible with the data for the case of a more realistic description of reflection, we repeated our spectral analysis while retaining the assumptions of model 2 but imposing the constraint $\mathcal{R} \geq 7$. This defines our model 5. The resulting fit provides a substantially worse description of the data, with $\Delta\chi^2 = 101$ (761 compared to 660 in model 2), and clear residuals appear around the Fe $K\alpha$ region, as shown in Fig. 8.

We have also considered a phenomenological spectral model that strictly follows the definition of the fully relativistic model in Steiner et al. (2024), as given in their Section 3.2.2. In this case, we find parameters similar to those reported in their Table 2, in particular $\mathcal{R} \approx 0.79$, which again does not support a strong dominance of reflection. When applied to our data, this model produces a residual pattern very similar to that shown in Fig. 3 of Steiner et al. (2024) and yields $\chi^2_\nu = 1036/644$. The spectral models developed here, therefore, provide a statistically better description of the data.

Parenthetically, we note that the dominance of reflection in the physical (i.e., computed with *kerrC* of Krawczynski 2012) model presented in Steiner et al. (2024) arises primarily from the local anisotropy of Comptonization rather than from light-bending effects. The fraction of photons returning to the disk depends on the radial emissivity profile and, even for extremely steep emissivities, remains below 50% (see, e.g., Fig. 4 in Riaz et al. 2021). In the *kerrC* setup, the radial emissivity of the corona closely follows that of the disk. Therefore, as in the case of disk emission, general-relativistic light bending and photon return can modify the flux by at most $\sim 10\%$, and thus cannot account for the dominance of reflection by a factor of ~ 7 . Comptonization in a slab corona irradiated from one side is intrinsically anisotropic, with the enhancement of the backscattered component increasing as τ decreases and as the seed-photon energy increases (e.g., Ghisellini et al. 1991; Haardt & Maraschi 1993). For $\tau = 0.007$ (as assumed in Steiner et al. 2024) and seed photon temperatures characteristic for a stellar-mass black-hole disk, the backscattered flux exceeds the forward-scattered flux by a factor of several, see Fig. 9a. This explains the strong

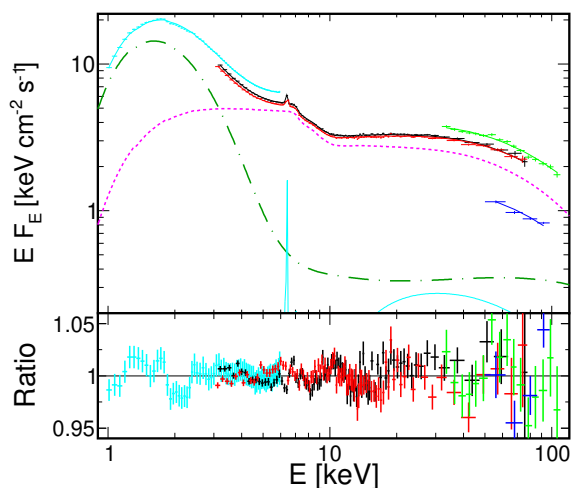


Fig. 8. Same as Fig. 3 but for model 5, i.e. with the constraint of $\mathcal{R} \geq 7$.

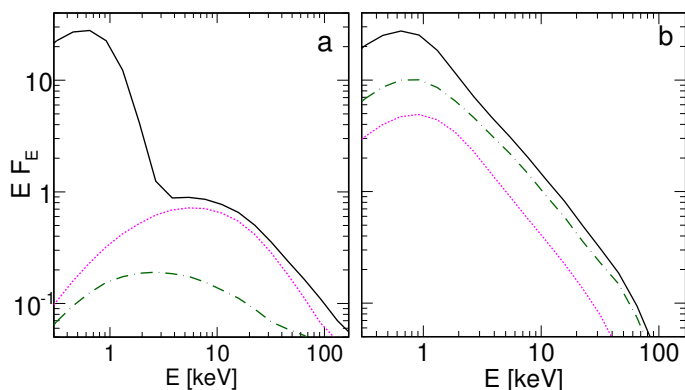


Fig. 9. Spectra observed at $i = 30^\circ$ from a disk-corona system for accretion-disk parameters corresponding to our model 3 and a slab corona with (a) $\tau = 0.007$ and $kT_e = 250$ keV, and (b) $\tau = 0.75$ and $kT_e = 25$ keV, computed using the Monte Carlo code of Niedźwiecki (2005). The solid curves show the total spectra, including the thermal disk emission. The dotted magenta curves represent the reflected component, and the dot-dashed green curves show the direct coronal emission. The reflection is calculated assuming a perfectly reflecting disk. For the non-rotating black hole adopted here, light-bending effects are negligible, and the difference between the reflected and direct components arises from local anisotropies of radiative processes.

dominance of reflection in the model in Steiner et al. (2024). By contrast, for $\tau > 0.1$ the local anisotropy becomes weak, see Fig. 9b, and arises mainly from scattering of reflected photons in the corona (an effect included in our spectral modeling).

Finally, we note that the model shown in Fig. 4 of Steiner et al. (2024) was computed using parameters $\dot{M} = 3.1 \times 10^{17}$ g s $^{-1}$ and $f_{\text{col}} = 1.8$ (Kun Hu, priv. comm.) for which the disk emission overpredicts the observed spectrum, and the peak of the returning component is shifted to ≈ 3 keV, compared to ≈ 2 keV in our best-fitting model. When we include in our model 1 a returning component calculated with those same parameters, we find that its contribution to the total PD in the 3–4 keV range increases from $\lesssim 25\%$ (in our fit-based model) to $\gtrsim 50\%$ (see the blue dotted curve in Fig. 7a). This likely accounts for the difference in our conclusions about the role of this effect.

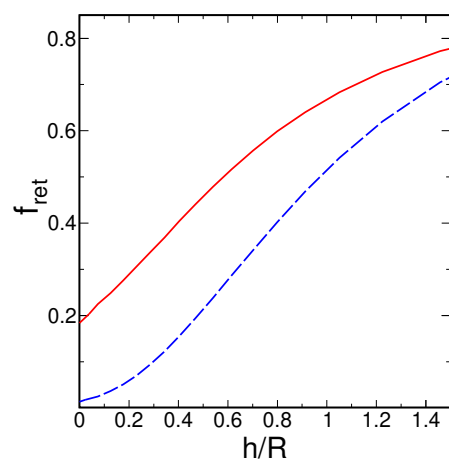


Fig. 10. Fraction of disk radiation returning to the disk versus disk aspect ratio for $a = 0$ (dashed blue) and $a = 0.998$ (solid red). The case $h = 0$ corresponds to an infinitesimally thin disk assumed in our main results.

4.4. Disk with non-zero thickness

Our calculations assume an infinitesimally thin accretion disk. If the outer disk is instead flared, the fraction of disk photons intercepted by the disk surface increases. In Fig. 10 we quantify this effect by showing the fraction of disk radiation returning to the disk as a function of the disk aspect ratio, h/R , where h is the half-thickness and R is the cylindrical radius. The estimate assumes that the angular distribution of the locally emitted radiation is not significantly altered by flaring, which is justified if the inner disk regions that dominate the luminosity remain only weakly flared. The effect shown in Fig. 10 arises from purely geometric shielding in flat spacetime and is unrelated to general-relativistic light bending. It depends only weakly on a . Consequently, the relative enhancement of returning radiation is larger for small a , where the return fraction related to general relativity is comparatively weak. We find that for a half-opening angle of $\gtrsim 50^\circ$, the reflected returning component could account for the observed polarization around ≈ 3 keV. However, even in this rather extreme configuration, it cannot reproduce the observed polarization spectrum, as its contribution declines rapidly with increasing photon energy and would produce a decreasing polarization, in contrast to the observed spectrum. Moreover, such a geometrically thick disk would subtend a solid angle corresponding to $\mathcal{R} \gtrsim 1.5$ at a central X-ray corona, implying a strong quasi-static reflection component. This substantially exceeds the limits on reflection obtained from our spectral analysis. We therefore conclude that this scenario is disfavored.

5. Summary and discussion

We performed a comprehensive analysis of the X-ray spectropolarimetric data of Cyg X-1 in the soft state, using convolution models for Comptonization and reflection that self-consistently account for the input photon energy distribution. We also applied our new model, `retBB`, which describes the disk thermal emission in a manner consistent with `kerrBB` and additionally incorporates the reflection of returning disk photons. Our study combines two methods for black-hole spin determination: disk-continuum fitting and relativistic reflection modeling. As in a similar analysis of an earlier 2019 Cyg X-1 soft-state observation (Zdziarski et al. 2024), we find that the inferred black-hole spin strongly depends on the adopted description of the thermal

component. When a warm, optically-thick layer Comptonizing the disk radiation is included, the spectral fit is consistent with a low spin value. At the fitted electron temperature of ≈ 0.5 keV, the warm layer is not fully ionized; therefore, the relativistic reflection inferred in our analysis may originate in this layer. If the warm layer is neglected, the spectral fit instead favors a near-extreme spin value.

For all our spectral decompositions, we calculated the expected polarization and found that, in our Cyg X-1 model, the polarization signal is dominated by the Comptonized component. However, the predicted PD is too low if the Comptonizing plasma corotates with the disk but has no bulk motion perpendicular to the disk plane. The predicted PD becomes consistent with the *IXPE* measurement if the plasma undergoes an outflow with a velocity of $\approx 0.3c$. Such an outflow also naturally explains the relatively weak relativistic reflection inferred from our spectral modeling, since the Doppler beaming away from the disk for $v = 0.3c$ corresponds to the reflection fraction $\mathcal{R} \approx 0.3$ (see, e.g., figure 1 of Beloborodov 1999) fitted in our models. Physical mechanisms that may drive this type of coronal outflow have been proposed in Beloborodov (1999, 2017).

While the spectral fits do not allow us to favor any particular spin value, the polarization measurements can provide a discriminant. Radiation from a disk-corona system around a rapidly rotating black hole exhibits a strong relativistic rotation of the PA, making it inconsistent with the observed polarization along the jet direction, and thus presumably perpendicular to the disk plane. Such rotation is expected whenever a significant fraction of the radiation originates within the central $\approx 5R_g$. For a slowly rotating black hole, the lack of such a contribution naturally follows from the standard assumption of weak energy dissipation within the ISCO. Therefore, the observed polarization favors a low spin value.

Our conclusions differ from those of Steiner et al. (2024) regarding the role of returning radiation. In particular, we find only a minor contribution of returning disk radiation even for high spin, in contrast to Steiner et al. (2024), who indicated this effect to be crucial. While the intrinsic polarization of the reflected returning disk component is indeed consistent with the observed PD and PA, its flux contribution is too small to play a significant role in explaining the measured signal. The discrepancy appears to arise from the fact that the polarization model presented in Steiner et al. (2024) was not strictly constrained by a spectral fit. We also do not confirm a significant role of light bending in producing the strong dominance of reflection over the direct coronal emission in their polarization model. For the extremely low optical depth assumed in that setup, the dominance of reflection is primarily a consequence of the local anisotropy of Comptonization rather than the effects of general relativity. Since the reflection component arises predominantly from local disk irradiation, its PD should be relatively low (compared to the $\sim 10\%$ polarization of returning disk-radiation reflection, which arises from grazing irradiation of distant regions of the disk).

On the other hand, our calculations of the polarization of the coronal reflection involve assumptions inherent to phenomenological reflection models, namely a radius-independent local reflection spectrum and locally isotropic disk irradiation. Both tend to suppress the predicted PD, and relaxing them would likely increase it moderately. Nevertheless, reflection cannot dominate the observed polarization, as spectral constraints require that its flux contribution remain relatively small.

An additional argument against attributing the observed polarization to reflection comes from the similarity of polarization signals across soft-state measurements (PA constant with energy

and PD increasing with energy; Kravtsov et al. 2025). This uniform behavior suggests a common physical mechanism operating in different sources. A reflection-dominated origin would generally imply strong reflection features in the energy spectrum. However, some sources observed in the soft state, such as 4U 1630–47, exhibit largely featureless spectra (Ratheesh et al. 2024). This favors Comptonization as the primary mechanism responsible for the observed polarization.

Finally, although our spectral fits include a non-thermal electron component contributing to the high-energy tail, our polarization calculations account only for the thermal electrons, due to current limitations of the `compps` model used here. In the fitted hybrid Comptonization models, the non-thermal tail contributes approximately 13% of the Compton-component energy flux in the 2–8 keV range. Its effect on the net polarization is therefore expected to be small. Consistent with this expectation, Beheshtipour et al. (2017) found that the non-thermal electron component has a negligible impact on the polarization properties of Comptonized emission in a hybrid plasma with parameters similar to those inferred from our spectral modeling.

Acknowledgements. We thank Henric Krawczynski and Kun Hu for discussions and Jack Steiner for providing the reduced NICER data. We acknowledge support from the Polish National Science Center grants 2023/50/A/ST9/00527, 2019/35/B/ST9/03944 and 2023/48/Q/ST9/00138. A.V. and J.P. are supported by the Research Council of Finland grants 355672, 372881, and the Centre of Excellence in Neutron-Star Physics (grant 374064). Nordita is supported in part by NordForsk. P.L. was partially supported by a program Regional Excellence Initiative (project no. RID/SP/0050/2024/1) of the Polish Ministry of Science.

References

- Agol, E. 1997, PhD thesis, University of California, Santa Barbara
- Agol, E. & Krolik, J. H. 2000, *ApJ*, 528, 161
- Arnaud, K. A. 1996, in *ASP Conf. Ser.*, Vol. 101, *Astronomical Data Analysis Software and Systems V*, ed. G. H. Jacoby & J. Barnes (San Francisco: Astron. Soc. Pac.), 17–20
- Beheshtipour, B., Krawczynski, H., & Malzac, J. 2017, *ApJ*, 850, 14
- Beloborodov, A. M. 1999, *ApJ*, 510, L123
- Beloborodov, A. M. 2017, *ApJ*, 850, 141
- Chandrasekhar, S. 1960, *Radiative transfer* (Oxford University Press)
- Connors, P. A., Piran, T., & Stark, R. F. 1980, *ApJ*, 235, 224
- Cunningham, C. 1976, *ApJ*, 208, 534
- Dauser, T., Wilms, J., Reynolds, C. S., & Brenneman, L. W. 2010, *MNRAS*, 409, 1534
- Dexter, J. 2016, *MNRAS*, 462, 115
- Done, C., Gierliński, M., & Kubota, A. 2007, *A&A Rev.*, 15, 1
- García, J., Dauser, T., Reynolds, C. S., et al. 2013, *ApJ*, 768, 146
- García, J. A., Dauser, T., Ludlam, R., et al. 2022, *ApJ*, 926, 13
- Ghisellini, G., George, I. M., Fabian, A. C., & Done, C. 1991, *MNRAS*, 248, 14
- Gierliński, M., Zdziarski, A. A., Poutanen, J., et al. 1999, *MNRAS*, 309, 496
- Haardt, F. & Maraschi, L. 1993, *ApJ*, 413, 507
- Kaastra, J. S. & Bleeker, J. A. M. 2016, *A&A*, 587, A151
- Kolehmainen, M., Done, C., & Díaz Trigo, M. 2011, *MNRAS*, 416, 311
- Kravtsov, V., Bocharova, A., Veledina, A., et al. 2025, *A&A*, 701, A115
- Krawczynski, H. 2012, *ApJ*, 754, 133
- Laor, A., Netzer, H., & Piran, T. 1990, *MNRAS*, 242, 560
- Li, L.-X., Zimmerman, E. R., Narayan, R., & McClintock, J. E. 2005, *ApJS*, 157, 335
- Loktev, V., Veledina, A., Poutanen, J., Näätäli, J., & Suleimanov, V. F. 2024, *A&A*, 685, A84
- Magdziarz, P. & Zdziarski, A. A. 1995, *MNRAS*, 273, 837
- Marra, L., Brigitte, M., Rodriguez Cavero, N., et al. 2024, *A&A*, 684, A95
- McConnell, M. L., Zdziarski, A. A., Bennett, K., et al. 2002, *ApJ*, 572, 984
- Miller-Jones, J. C. A., Bahramian, A., Orosz, J. A., et al. 2021, *Science*, 371, 1046
- Niedźwiecki, A. 2005, *MNRAS*, 356, 913
- Niedźwiecki, A., Szanecki, M., & Zdziarski, A. A. 2019, *MNRAS*, 485, 2942
- Novikov, I. D. & Thorne, K. S. 1973, in *Black Holes (Les Astres Occlus)*, ed. C. Dewitt & B. S. Dewitt, 343–450
- Page, D. N. & Thorne, K. S. 1974, *ApJ*, 191, 499
- Phlips, B. F., Jung, G. V., Leising, M. D., et al. 1996, *ApJ*, 465, 907
- Poutanen, J. & Svensson, R. 1996, *ApJ*, 470, 249

- Poutanen, J., Veledina, A., & Beloborodov, A. M. 2023, *ApJ*, 949, L10
- Ramachandran, V., Sander, A. A. C., Oskinova, L. M., et al. 2025, *A&A*, 698, A37
- Ratheesh, A., Dovčiak, M., Krawczynski, H., et al. 2024, *ApJ*, 964, 77
- Riaz, S., Szanecki, M., Niedźwiecki, A., Ayzenberg, D., & Bambi, C. 2021, *ApJ*, 910, 49
- Schnittman, J. D. & Krolik, J. H. 2009, *ApJ*, 701, 1175
- Sobolev, V. V. 1963, *A treatise on radiative transfer* (Princeton: Van Nostrand)
- Steiner, J. F., Nathan, E., Hu, K., et al. 2024, *ApJ*, 969, L30
- Svoboda, J., Dovčiak, M., Steiner, J. F., et al. 2024, *ApJ*, 960, 3
- Walton, D. J., Tomsick, J. A., Madsen, K. K., et al. 2016, *ApJ*, 826, 87
- Weisskopf, M. C., Soffitta, P., Baldini, L., et al. 2022, *JATIS*, 8, 026002
- Wilms, J., Allen, A., & McCray, R. 2000, *ApJ*, 542, 914
- Zdziarski, A. A., Chand, S., Banerjee, S., et al. 2024, *ApJ*, 967, L9
- Zdziarski, A. A. & Gierliński, M. 2004, *Progress of Theoretical Physics Supplement*, 155, 99
- Zdziarski, A. A., Szanecki, M., Poutanen, J., Gierliński, M., & Biernacki, P. 2020, *MNRAS*, 492, 5234

Appendix A: retBB

Our new model, `retBB`, extends the `reflkerr` family of models (Niedźwiecki et al. 2019), by incorporating the reflection of the returning blackbody photons and accounting for the polarization of the reflected and direct emission from an accretion disk. We assume that a flat accretion disk is located in the equatorial plane of a Kerr black hole characterized by the dimensionless angular momentum a and mass M . The inclination angle of the line of sight to the symmetry axis is given by i . All `retBB` results presented in this work (except for the green dotted curve in Fig. A.4) are for the outer radius of $R_{\text{out}} = 10^3 R_g$. We use the formula of Page & Thorne (1974) for the local radiative flux from a disk accreting at a rate \dot{M} for a zero-stress inner boundary condition at the ISCO, \mathcal{F} , which determines the local effective temperature $T_{\text{eff}} = (\mathcal{F}/\sigma_{\text{SB}})^{1/4}$, where σ_{SB} is the Stefan-Boltzmann constant. We approximate the local spectrum of the quasi-thermal emission by a diluted blackbody, with the spectral intensity $I_\nu(\mu) = I_{\text{limb}}(\mu) f_{\text{col}}^{-4} B_\nu(f_{\text{col}} T_{\text{eff}})$, where B_ν is the Planck function, $\mu = \cos \theta$, θ is the emission angle with respect to the normal to the disk measured in the disk rest frame, and I_{limb} is the limb darkening/brightening factor for a plane-parallel, electron scattering-dominated atmosphere tabulated as a function of μ in Table XXIV in Chandrasekhar (1960). For the local polarization of the thermal disk emission, we use the polarization degree given in the same Table XXIV; it ranges from PD = 0 to $\approx 12\%$ for photons emitted normal and parallel, respectively, to the disk surface.

The flux of radiation seen by a distant observer is computed by means of a photon transfer function, \mathcal{T} ,

$$F(E_{\text{obs}}, i) = \int \mathcal{T}(a, r, \theta, \phi, i, g) I\left(\frac{E_{\text{obs}}}{g}, r, \theta\right) 2\pi r dr d\phi d\mu dg, \quad (\text{A.1})$$

where $g = E_{\text{obs}}/E_{\text{disk}}$. We assume local azimuthal symmetry of the thermal emission, so the intensity I in Eq. A.1 does not depend on the azimuthal emission angle in the disk frame, ϕ . However, we use a ϕ -dependent transfer function because it is also applied to the reflected radiation, for which azimuthal symmetry does not necessarily hold. The observed Stokes parameters are computed using analogous transfer functions, \mathcal{T}_X and \mathcal{T}_Y . The transfer functions \mathcal{T} , \mathcal{T}_X and \mathcal{T}_Y are defined in the same way as in Laor et al. (1990) and treat the effects of special and general relativity on the observed total and polarized radiation. We construct them by following a large number of photon trajectories originating in the disk until they are captured by the black hole, return to the disk plane, or reach a distant observer. We compute the photon trajectories using the code employed for the transfer functions of the other `reflkerr` models, to which we have added a description of the photon beam polarization, based on the methodology developed in Connors et al. (1980), Agol (1997) and Dexter (2016). In it, the parallel transport of the polarization vector along the null geodesic is calculated using the Walker-Penrose integral of motion, which allows the reconstruction of the polarization vector at any point along the geodesic.

Trajectories of photons returning to the disk are tabulated to construct the transfer functions for returning radiation $\mathcal{T}_{\text{ret}}(r, \mu, \varphi, r_{\text{in}}, \mu_{\text{in}}, \varphi_{\text{in}}, g)$, $\mathcal{T}_{X,\text{ret}}(r, \mu, \varphi, r_{\text{in}}, \mu_{\text{in}}, \varphi_{\text{in}}, g)$ and $\mathcal{T}_{Y,\text{ret}}(r, \mu, \varphi, r_{\text{in}}, \mu_{\text{in}}, \varphi_{\text{in}}, g)$, where μ_{in} , φ_{in} and r_{in} are the incidence angles and the incidence radius. Convolution of these transfer functions with the disk thermal spectrum yields the spectrum and polarization of the radiation returning to the disk. Scattering of this radiation off the disk surface is calculated using the

transfer matrix for reflection defined in Section 70.3 and given in Table XXV of Chandrasekhar (1960). The reflected radiation is then convolved with \mathcal{T} , \mathcal{T}_X , and \mathcal{T}_Y to find the observed spectrum and polarization of this reflected component. The `retBB` model may apply the spectral modification due to atomic processes, for which the `xillverNS` table model is used. However, note that this only modifies the spectral shape, while the polarization state remains described by Chandrasekhar's model of elastic reflection. This approach overestimates the polarization of the fluorescent and free-free component of the reflected radiation.

Figures A.1 and A.2 show example energy and polarization spectra for the parameters relevant to Cyg X-1. Note that the clockwise disk rotation assumed here is opposite to the counterclockwise rotation usually adopted in theoretical studies⁴. Also note that our definition of PA differs from, e.g., Schnittman & Krolik (2009), who measure it from the direction parallel to the disk. We note an overall good qualitative agreement with previous studies of the polarization of Kerr black-hole disks (Connors et al. 1980; Laor et al. 1990; Schnittman & Krolik 2009). At low energies, the direct disk component is dominated by emission from large radii, with the PD given by the Chandrasekhar result. At higher energies, the inner regions of the disk dominate, and relativistic effects reduce the PD. The most significant of these effects is the gravitational rotation of polarization planes, corresponding to the bending of photon trajectories. Combining photon beams with differently rotated polarization planes decreases PD, as can be seen from the red dotted curves in Figs. A.1 and A.2. Similar depolarization is not significant for the returning component, as it arises from a much narrower radius range. For this component, the bending of trajectories may affect the polarization by combining photons emitted at different θ , which are differently polarized; this effect increases the PD to more than 10% at $E > 10$ keV for the first order reflection in Fig. A.1. The total polarization transitions from a direct flux contribution that dominates at low energies and produces horizontal polarization, to a returning polarized flux contribution that dominates at higher energies and produces net vertical polarization. When this transition occurs, the PD passes through a minimum, as the two contributions cancel each other out.

Figure A.1 also illustrates the effect of higher-order reflection. For very high values of a , these produce a tail extending to several hundred keV with a photon index of $\Gamma \sim 3$. The intensity of this component is very low and, even for $a = 0.998$, it contributes negligibly to the high-energy tail observed in the soft state of Cyg X-1. It could, however, be relevant in very soft states where only weak high-energy tails above the disk spectrum are present. Even in that case, its contribution to the polarized flux within the *IXPE* energy band remains negligible.

As in previous studies, we considered only the reflection of radiation returning beyond the ISCO. Figure A.2 shows that reflection within the ISCO for $a = 0$ is not a significant effect, and even including it, the returning component is much too weak to be measured in any real system hosting a slowly rotating black hole. Including the reflection within the ISCO also slightly decreases the energy at which the polarization swings from horizontal to vertical.

We now quantitatively compare `retBB` with the available predictions of other models. We first note that, for $a = 0.998$, we find that $\approx 20\%$ of the disk radiation returns to the disk,

⁴ We remind that in our notation $i = 180^\circ - i_{\text{orb}}$, where i_{orb} denotes the binary inclination.

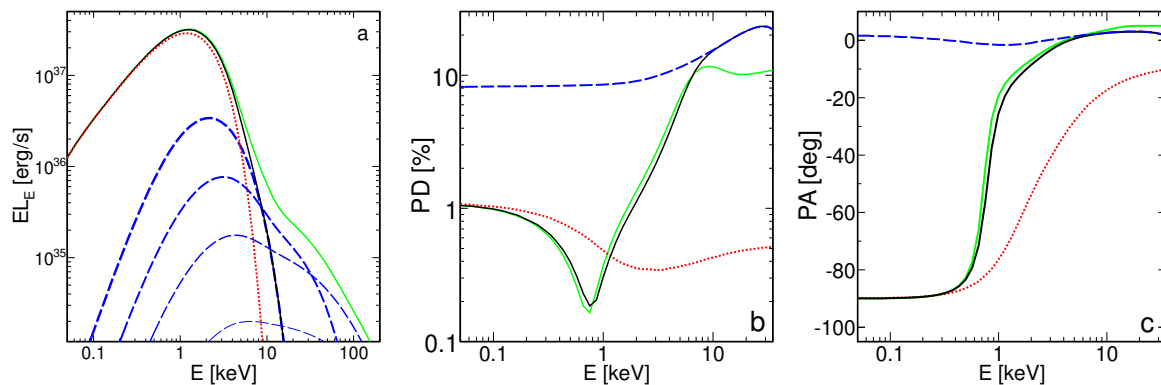


Fig. A.1. Observed spectrum, polarization degree and angle predicted by `retBB` for $a = 0.998$, $M = 21.2M_{\odot}$, $\dot{M} = 2.5 \times 10^{17} \text{ g s}^{-1}$, $i = 45^{\circ}$ and $f_{\text{col}} = 1.5$. (a) The red dotted curve shows the spectrum of the direct disk emission. The blue dashed curves from top to bottom show spectra of the first to fourth orders of elastic reflection of the returning radiation. The solid black and green curves show the total spectrum, including single- and multiple-scattering (up to fourth order) of the returning radiation, respectively. (b) and (c) PD and PA, including a single (black solid) or multiple (up to the fourth order; green solid) reflection of returning radiation; blue dashed and red dotted curves show contributions of the first order reflection and direct disk radiation, respectively.

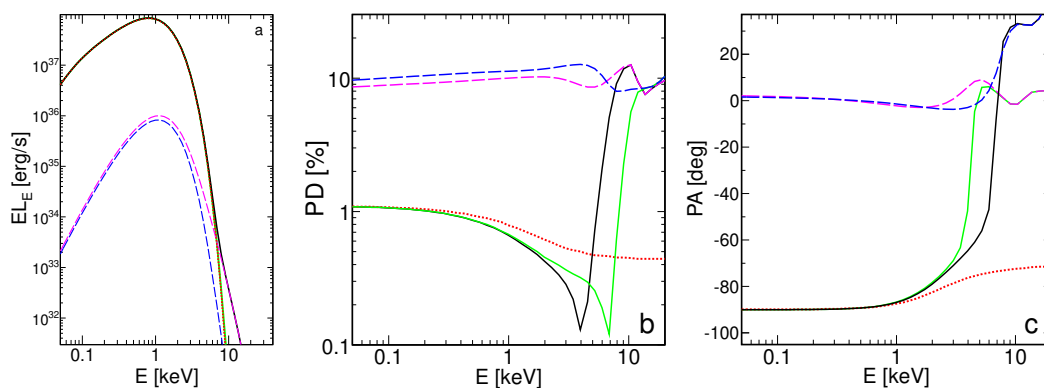


Fig. A.2. Observed spectrum, polarization degree and angle predicted by `retBB` for $a = 0$, $M = 21.2M_{\odot}$, $\dot{M} = 2.5 \times 10^{18} \text{ g s}^{-1}$, $i = 45^{\circ}$ and $f_{\text{col}} = 1.5$. (a) The red dotted curve shows the spectrum of the direct disk emission. The blue and magenta dashed curves show the elastic reflection of the returning radiation, excluding and including, respectively, the reflection inside ISCO. The spectra include multiple reflections; however, contributions beyond the first order are negligible. The solid black and green curves show the total spectrum without and with reflection inside the ISCO, respectively. (b) and (c) The corresponding PD and PA, the color scheme follows panel (a).

120 which agrees with previous estimates (e.g., Agol & Krolik 2000; Li et al. 2005). Figure A.3 compares the energy spectra predicted by `retBB` with those computed by Schnittman & Krolik (2009), digitized from their paper using WebPlotDigitizer.⁵ Both models include multiple elastic reflections. We initially adopted the Eddington fractions reported in that work ($L = 0.1L_{\text{Edd}}$), but found discrepancies in the shapes of the direct disk spectra (while `retBB` fully agrees with `kerrbb`). Only a rough match could be achieved, requiring setting in `retBB` very low accretion rates corresponding to disk luminosities of $< 10^{-3}L_{\text{Edd}}$; these matched spectra are shown in Fig. A.3. After normalizing the direct spectra, the luminosities of the reflected returning components agree within a factor of ~ 2 . However, in Schnittman & Krolik (2009) this component is generally weaker and, for $a = 0.998$, extends to much lower energies than in `retBB`.

130 We now compare `retBB` with `kerrC` of Krawczynski (2012). The published `kerrC` results do not separate the direct and reflected components, preventing a comparison of energy spectra like those in Fig. A.3. Figure A.4 compares the PDs predicted by the two models. We find moderate differences between `retBB` and `kerrC`, with the latter extracted from the PD-plots of Krawczynski (2012) using WebPlotDigitizer. At low energies,

the Chandrasekhar limit, $\text{PD} \simeq 4.5\%$ for $i = 75^{\circ}$, should be recovered. This is satisfied by `retBB`, whereas `kerrC` slightly underpredicts PD, likely due to assuming a relatively small outer radius ($R_{\text{out}} = 100$). This effect is illustrated by the green dotted `retBB` curve. For the parameters considered here, differences related to R_{out} affect only energies below the *IXPE* band.

⁵ <https://automeris.io>

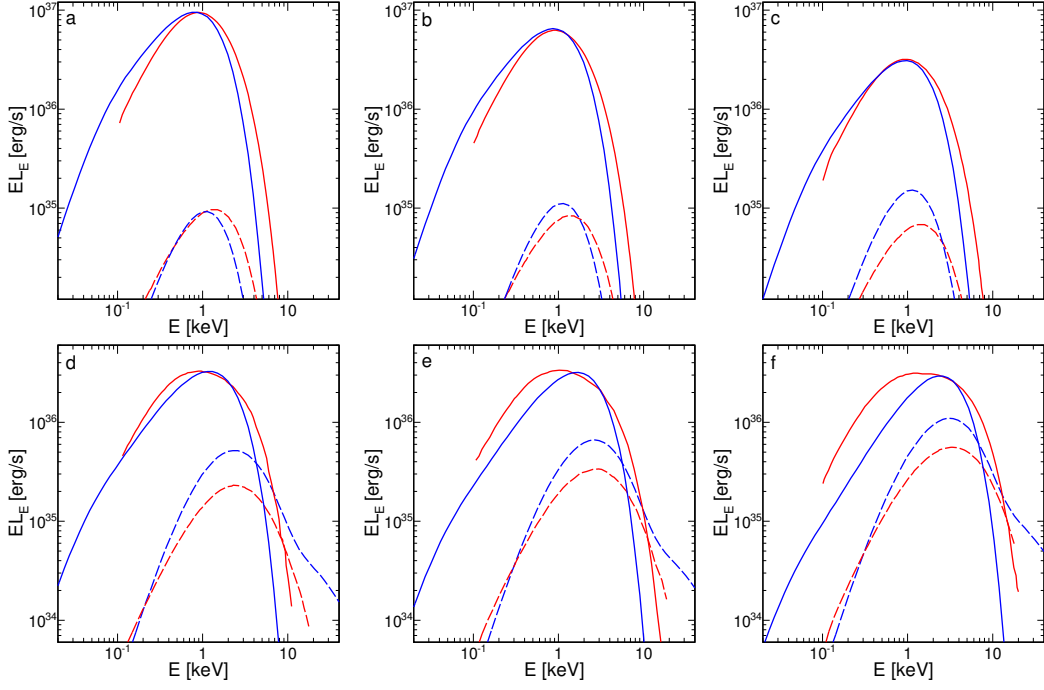


Fig. A.3. Comparison of the spectra predicted by `retBB` (blue curves) and Schnittman & Krolik (2009) (red curves) for $M = 10M_{\odot}$, $f_{\text{col}} = 1.8$ and $i = 45^{\circ}$, 60° and 75° from left to right. In all panels, the solid curves show the direct disk radiation and the dashed curves show the elastic reflection of the returning radiation. The top panels are for $a = 0$, the Schnittman & Krolik (2009) spectra are read from the left column of their figure 4, and $\dot{M} = 0.2L_{\text{Edd}}/c^2$ is assumed in `retBB` to approximately match the shape thermal disk component of Schnittman & Krolik (2009). The bottom panels are for $a = 0.998$, the Schnittman & Krolik (2009) spectra are read from the left column of their figure 6, and $\dot{M} = 0.02L_{\text{Edd}}/c^2$ is assumed in `retBB` to approximately match the shape of the thermal disk component of Schnittman & Krolik (2009).

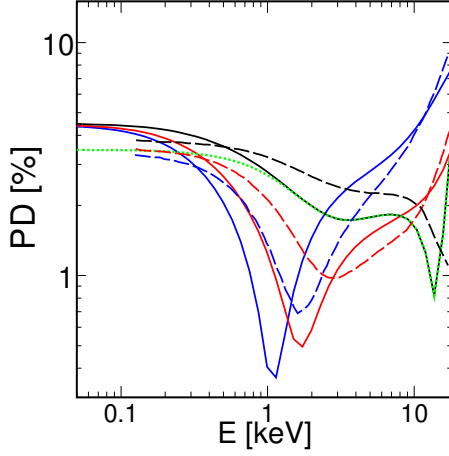


Fig. A.4. Comparison of the polarization degrees predicted by `retBB` and `kerrC`. The dashed curves show PD given in figure 5 of Krawczynski (2012) for $a = 0$ (black), $a = 0.9$ (red) and $a = 0.99$ (blue). The solid curves show the PD predicted by `retBB` for the same parameters ($i = 75^{\circ}$, $f_{\text{col}} = 1.8$, $M = 10M_{\odot}$, $\dot{M} = 2.45 \times 10^{18} \text{ g s}^{-1}$ for $a = 0$, $\dot{M} = 9 \times 10^{17} \text{ g s}^{-1}$ for $a = 0.9$ and $\dot{M} = 5.3 \times 10^{17} \text{ g s}^{-1}$ for $a = 0.99$) for a single elastic reflection (using a multiple reflection does not improve the agreement). The green dotted curve shows the `retBB` spectrum with $R_{\text{out}} = 100$.